Source Characteristics of the 2016 Meinong (M_L 6.6), Taiwan, Earthquake, Revealed from Dense Seismic Arrays: Double Sources and Velocity Pulse-like Ground Motion

by Yen-Yu Lin, Te-Yang Yeh, Kuo-Fong Ma, Teh-Ru Alex Song, Shiann-Jong Lee, Bor-Shouh Huang, Yih-Min Wu

Corresponding author: Yen-Yu Lin
Email address: yylinm22@gmail.com
Tel: +1-626-395-3861
Mailing address: 1200 E. California Blvd., MS252-21, Pasadena, CA 91125, USA

Abstract

The February 5, 2016 (UT), Meinong, Taiwan, earthquake, brought extensive damage to nearby cities with significant velocity pulse-like ground motions. In addition to the spatial slip distribution determination using filtered strong motion data, we show that on the advantage of the densely distributed seismic network as a seismic array, we can project the earthquake sources (asperities) directly using nearly unfiltered data, which is crucial to the understanding on the generation of the velocity pulse-like ground motions. We recognize the moderate but damaging M_L 6.6 Meinong earthquake was a composite of an M_W 5.5 foreshock and M_W 6.18 mainshock with a time delay of 1.8–5.0 s. The foreshock occurred in the hypocenter reported by the official agency, following by the mainshock centroid occurred 12.3 km to the north north-west of the hypocenter and at a depth of 15 km. This foreshock-mainshock events are non-distinguishable as it was buried as one event, while using low-frequency filtered seismic data for the finite-fault inversion. Our results show that the velocity pulse-like ground motions are mainly resulted from the source of mainshock with its directivity and site effects, resulting in the disastrous damages in Tainan City. Although finite-fault inversion using filtered seismic data for spatial slip distribution on the fault has been a classic procedure in understanding earthquake rupture processes, using a dense seismic network as a seismic array for unfiltered records helps us delineate the earthquake sources directly and provide more delicate information for future

understanding on earthquake source complexity.

Introduction

A moderate earthquake, M_L 6.6, struck southern Taiwan on February 5, 2016 (UT). It was the island of Taiwan's largest earthquake causing inland damage since the 1999 Chi-Chi earthquake, M_W 7.6. According to the Central Weather Bureau's (CWB) official agency report, the earthquake occurred at location E120.5438°, N22.9220°, with a focal depth of 14.6 km, in the Meinong district of Kaohsiung City (Fig. 1). This event caused 117 casualties, 551 injuries, and 412 collapsed and damaged buildings. Most of the destruction was located near Tainan City rather than the epicenter, the Meinong area (Figs. 1 and 2). Fig. 2 shows the distribution of peak-ground acceleration (PGA) and peak-ground velocity (PGV) with the seriously damaged buildings (green squares), which confirmed that the largest shaking and velocity region was very close to Tainan City. The damages and fatalities caused by this moderate-size earthquake with moderate focal depth surprised the community. It requires further attention to understand future seismic hazards.

Seismologists commonly determine source characteristics for moderate to large earthquakes by the finite-fault inversion technique. They assume a fault plane based on an obtained focal mechanism and calculate Green's functions for geophysical records (e.g. seismic waveforms) on each subfault within the entire fault plane. Thus, they can solve the slip distribution and its history of an earthquake on the fault plane by the inversion technique. Since the limitation of the velocity structure, only low-frequency geophysical records (< 0.5 Hz) are applied in the finite-fault inversion. Source characteristics of the Meinong earthquake have been determined by using low-frequency geophysical records (e.g., seismic waveforms and Global Positioning System [GPS] records). Lee et al. (2016) estimated the focal mechanism by the real-time moment tensor (RMT) inversion technique and determined the co-seismic slip characteristics by considering a joint inversion technique combining teleseismic, local strong-motion records, with frequency bands lower than 0.33 Hz (3 s), and GPS data. Kanamori et al. (2016) obtained a co-seismic slip model through a finite-fault inversion technique by using the teleseismic records in frequency bands from 2–30 s. Their results indicated that the centroid of the Meinong earthquake was located ~10 km north north-west of the epicenter reported by the CWB. They both concluded that the unexpected large ground motions that appeared in Tainan City were because of the combination of strong directivity, radiation pattern, and site amplification. According to their moment tensor solutions, the Meinong earthquake could have ruptured either the northwest-southeast low-angle plane or the north-south high-angle plane (Fig. 1). They preferred the low-angle plane with a strike-slip mechanism.

Furthermore, Jian et al. (2017) analyzed high-frequency P wave (0.5–1.5 Hz) teleseismic records for dense seismic networks in Europe and Australia and used a back-projection technique tracking the details of the rupture process. Their result indicated a rupture pattern similar to the results from the finite-fault inversions, going from the CWB epicenter to the northwest with an average rupture speed of 2.4 km/s.

Since 2013, Taiwan has operated an on-site P-alert Earthquake Early Warning (EEW) system, which has functioned well in alerting residents about local events (Wu et al., 2013). The P-alert system (~600 stations as of 2017) uses low-cost strong motion sensors, which are typically installed on the first or second floor of elementary schools in Taiwan. It was a surprise that this low-cost strong motion sensor also records high-quality strong motion waveforms. We demonstrate the capability of these densely populated stations as well as other free-field stations, mainly from the P-alert system (see Wu et al., 2016 for more details), and use them as a seismic array to study the source of the Meinong earthquake. This dense seismic array allows us to study the earthquake without distortion from filtering the data. We are thus able to untangle the M_L 6.6 Meinong earthquake as an event doublet, with an M_W 5.5 foreshock a few seconds ahead of the M_W 6.18 mainshock, in a blind fault system, using source-scanning algorithm technique. What caused the severe damage to Tainan City and the nearby region is due to the close-in large short-duration velocity pulses generated by the single source of the M_W 6.18 mainshock. This is typically as referred to be the velocity pulse-like ground motion, in earthquake engineering (Hall et al., 1995; Heaton et al., 1995).

The velocity pulse-like ground motion is often characterized by a pulse wave of 1–2 seconds period with large amplitudes, causing tremendous damages to buildings (Heaton et al., 1995). It is believed to be caused by near-fault forward directivity effect (Somerville et al., 1997; Somerville, 2003; Baker, 2007; Shahi and Baker, 2011). The collapse of a high-rise building that caused 115 deaths and of numerous other buildings in the western area of the Meinong earthquake brought attention to the generation of the velocity pulse-like ground motion that was considerably responsible for the damage. The velocity pulse-like ground motion observed in the 1994 Northridge and 1995 Kobe earthquakes has been shown to have significantly impact to earthquake hazards. The velocity pulse appears to be important for earthquake engineering because when coupled with a large displacement peak, it could seriously damage buildings (Hall et al., 1995). Cox and Ashord (2002) analyzed the near-field records from 15 large earthquakes. They summarized that the conditions for producing a large velocity pulse include 1) the earthquake is larger than M_W 6.0; 2) the site is close to the fault, within 10 km; and 3) the rupture propagates toward the site. The generation of the velocity pulse-like ground motion of 2016 Meinong earthquake are intriguing, as the observed velocity pulse-like ground motions were not identified as either near the fault or close to the hypocenter from rapid spatial slip distribution. The in-depth examination of waveforms from the dense seismic network allows us to decipher the generation of the velocity pulse-like ground motion. Despite the fact of the dense P-alert seismic network for EEW, we note the surprising high quality performance in waveforms of the low-cost P-alert EEW system, which greatly helps to understand earthquake source complexity.

Data

We analyze seismic waveforms from three seismic networks in Taiwan: 1) the Broadband Array in Taiwan for Seismology (BATS), operated by the Institute of Earth Science (IES), Academia Sinica, Taiwan, 2) the Real-Time Data network (RTD), managed by the CWB, and 3) the P-alert network, conducted by National Taiwan University (NTU). The instruments of the RTD and P-alert were accelerometers, and the instrument response was flat between 0.07 and 10 Hz. In the BATS network, both broadband seismometers and accelerometers were deployed in the same locations. The sampling rate was 100 samples per second for all stations. Clocks on the instruments for BATS and RTD were calibrated by GPS, and were done by Network Time Protocol through the Internet for P-alert. Since the purpose of the present study is to understand the source process from nearby stations, we selected only the stations in southern Taiwan (latitude < N23.5°) with good azimuthal coverage (Fig. 1), including 3 stations from BATS (triangles), 29 from RTD (diamonds), and 91 from P-alert (squares), which are 122 stations in total. We discard records with drifting noise or saturation. Although the P-alert network is not free-field stations, a test on the performance of this system against free-field stations shows almost no amplification and waveform distortion with respect to the recordings in the free-field stations. This also could be seen in Figs. 3 and 4 for the good correlation of the P-alert strong motion data to those from free-field stations as BATS and RTD.

Identification of two sources from the waveform travel-time curve

To determine the far-field term of the earthquakes, we obtain displacement waveforms from the acceleration records by double integrations. To avoid drifting during the integrations, we apply a zero-phase high-pass filter with a corner of 0.1 Hz to the data. We display the displacement record session against the epicenter and the origin time of the Meinong earthquake determined from the CWB report. Three component record sections, including stations in the south (the squares in red frames in Fig. 1), are shown in Figs. 3(a–c), for Z, N, and E components, respectively. To examine the waveforms from travel-time curves, we calculate the theoretical P- and S-wave arrival times (P1 and S1 phases as T1 and T2 markers shown in Fig. 3) from the hypocenter reported by the CWB using a Taiwan 3D velocity model (H14-3D) of Huang et al. (2014). This velocity model has a near-surface shallow velocity structure constrained from drilling logging data to provide a more reliable velocity layer near the surface.

We observe that obvious, stronger, and lower frequency phases appear ~5.0 s after the S1 phases in the record sections (Figs. 3a–c). The apparent velocity of these phases is similar to the velocity of the S1 phases, suggesting that these phases propagate by S-wave velocity. We call this phase S2 in the following study. Similarly, we identify clear and longer period phases (called P2) propagating at the P-wave speed (Figs. 3d–e), which appears ~5.0 s after the P1 phases between the P1 and S1 phases. The moveout of picked arrival times for P1, P2, S1, and S2 phases are shown in Fig. 3g. Since the delay times (~5.0 s) of P2-P1 and S2-S1 pairs are so similar, it is very likely that the P2-S2 pair is attributed to another seismic source located somewhere else rather than the source at the hypocenter with a few seconds of delay time. For the difference in amplitude and origin time of these two sources, we separate them from the Meinong earthquake rupture history and refer the first source as the foreshock and the second source as the mainshock.

Location of the mainshock

Since the temporal separation between the two events was only several seconds, it is challenging to detect both events for the routine determination of earthquake location and magnitude such as the CWB report, which is based on information from less-populated seismic stations. We improve a source-scanning algorithm technique (SSA) described in Kao and Shan (2004) to determine the location of the mainshock to resolve the complexity in P2- and

S2-pickings. The SSA method was successfully applied to the locations of events with ambiguous first arrivals, such as the distribution of the episodic tremor and slip sequence determination in the northern Cascadia subduction zone (Kao and Shan, 2004), and the rapid identification of fault planes for earthquakes (Kao and Shan, 2007; Kao et al., 2008). It was also used for the delineation of source characteristics of earthquake doublets (Kan et al., 2010), near-real-time epicentral determination of landslides (Kao et al., 2012), and location estimation of the earthquakes observed by the Ocean Bottom Seismometers network offshore southern Taiwan (Liao et al., 2012).

We slightly modify the current SSA method to determine the most likely location of the mainshock as well as its uncertainty simultaneously. The idea is to convert each displacement waveform to a probability density function (PDF), representing the distribution of seismic energy as a function of time. To convert seismic waveforms into PDFs, we integrate acceleration records to displacement, apply a zero-phase high-pass filter with a corner of 0.1 Hz to avoid drifting, square the amplitude to make it positive, and scale the squared amplitudes so that the area beneath the function is one. Since our goal is to determine the location of the source that caused the large pulse in horizontal components, only E-W and N-S components are used in the following analysis.

The SSA is a grid-search method for determining optimal distribution of the source location based on the seismic waveforms. The SSA method described in Kao and Shan (2004) stacked all normalized waveforms and calculated the "brightness" of an assumed source point (η) at a specific delay time (τ). The source location was determined to be in the maximum brightness location. In the modified version of SSA, we compute probabilities of a proposed source location and delay time from each PDF by summing the amplitudes in the predicted time window. It is noted that the predicted time window has a certain width so that it can accommodate the errors from inaccurate travel-time prediction. We define the brightness function for the modified SSA as the product of the probabilities computed from all the PDFs, which is equivalent to the likelihood of the proposed model,

$$br(\eta,\tau)=\prod_{n=1}^{N}\sum_{m=-M}^{M}\left|P_n(\tau+t_{\eta n}+mdt)\right|, \qquad (1)$$

where P_n is the PDF converted from seismic trace n. $t_{\eta\tau}$ is the predicted travel time for S wave from point η to station n. $2M$ is the number of points within the time window centered around the predicted arrival time, and dt is the sampling rate.

We calculate the brightness from the records of all stations in section "Data" except the stations with bad data quality, such as disconnection due to large shaking, which results in 113 stations total. We search the potential source area from longitude E120.20° to 120.80° and latitude N22.60° to 23.20° with a 0.025° interval in both directions. The depth grids are from 5.0 to 30.0 km with a 2.5 km interval. The delay times range from 0.0 to 10.0 s with a 0.05 s interval.

The predicted S-wave travel times $t_{\eta\tau}$ are calculated based on the H14-3D model. According to the residuals of S-wave arrival times in the model (Huang et al., 2014), we consider a time window of ±1.0 s (M = 100) when computing the probabilities. As a result, we derived a multidimensional likelihood function that could be considered as an approximation of the posterior probability distribution of the model parameters. The maximum likelihood centroid location and delay time of the mainshock are therefore determined.

To test the resolution of the improved SSA method, we produce pulse-like displacement records with a 1.5 s duration representing P- and S-waves at all stations with a 5.0 s centroid delay. The arrivals of P and S waves are predicted based on the H14-3D model, noted that we add uniformly distributed random travel time residuals ranging in ±1.0 s. 20% maximum amplitude random noises are considered in the synthetics. Following the same data processing we mentioned previously, the test results indicate that this method can determine the source location and timing accurately (Fig. S1). We further compare the results analyzed by real data between the improved and original SSA methods. The results reveal that the improved SSA method indeed improves both spatial and temporal resolution compared to the original SSA method (Fig. S2).

The maximum probability in space of the mainshock centroid is determined to be at a location (E120.500°, N23.025°) that is 12.3 km north north-west of the CWB epicenter where there is a blank zone of the aftershocks (Fig. 5a). The focal depth is 15 km, as shown in Fig. 5b. Based on the location and the delay time 5.3 s of the mainshock centroid estimated above, the corresponding P1, S1, and P2, S2 for the foreshock and mainshock are clearly identified accordingly from the waveforms in an E-W component for the stations in the south, west, north, and east (Fig. 4). These arrival pairs are consistent with the observations in the travel-time curve shown in Fig. 3. The stations in the southern region show the most evidence of the corresponding P- and S-wave pairs for their backward direction to the foreshock and mainshock. Due to complex structures beneath the Central Range, the mainshock centroid times and the waveforms in some stations in the east become less visible.

We further compare the solutions of the Meinong earthquake location from different analyses based on different datasets—CWB, P-alert, RMT, W-phase, and Global Centroid Moment Tensor (GCMT)—shown in the green symbols in Figs. 5(a–b). These are the first-hand information of the Meinong earthquake for the public. The solutions estimated by P-wave arrival-time information from the local networks, such as the CWB (the star) and P-alert (the diamond), distribute close to the CWB epicenter. However, the solutions determined by the waveform inversion techniques based on only teleseismic data (GCMT) or regional records (RMT and W-phase) are grouped in the northwest region, where the SSA technique located the mainshock. It suggests that the methods using the waveform inversion techniques or using teleseismic records have difficulty recognizing the event doublet because of insufficiency of the frequency band in high frequencies as we suggested earlier. The results from waveform inversion and teleseismic waveforms are mainly for the mainshock we identified in the present study.

In Fig. 5(c) we identify that the maximum probability of delay time for the mainshock centroid is at 5.3 s. Since the estimated delay time indicates a centroid delay of the mainshock compared to the origin time of the Meinong earthquake (the foreshock), we do not know the precise origin time of the mainshock. We calculate the centroid delay to be ~3.5 s for an M_W 6.18 earthquake following the relation described from Duputel et al. (2013). Therefore, the origin time difference between both events should be longer than 1.8 s. Since we knew that the mainshock location was in the north of the foreshock, the determined ~5.0 s delay of P2-P1 and S2-S1 phases in the stations in the south in section "Identification of two sources from the waveform travel-time curve" should include a longer propagating path and time than the source at the hypocenter. Therefore, the exact origin time delay of the mainshock should be less than 5.0 s. We thus recognize the origin time of the mainshock should be 1.8–5.0 s later than the foreshock.

Magnitudes and focal mechanisms of the foreshock and the mainshock

The short separation in time (1.8–5.0 s) between both events makes it difficult to identify the waveforms and estimate source parameters (e.g., magnitude and focal mechanism) for the buried event precisely. In this section, we discuss using the waveforms from the southern stations (e.g., MASB station) that have clear P1 and S1 phases to estimate the magnitude and focal mechanism of the foreshock.

To separate the foreshock signals from the waveforms, we compare the unfiltered velocity waveforms of MASB station in the E-component of the Meinong earthquake and a nearby smaller earthquake, M_W 5.05, event from December 23, 2008, (E2008) as shown in Fig. 6(a). The magnitude and focal mechanism of the E2008 event were estimated by moment tensor inversion. The location of the E2008 earthquake and its focal mechanism, which is similar to the Meinong earthquake, are shown in Fig. 5(a). In Fig. 6(a), we mark the P1, S1, P2, and S2 arrivals on the waveform of the Meinong earthquake and also show the P- and S-wave arrivals for the small earthquake on the records for the reference. All phases in the Meinong records are recognized clearly except the P2 phase, which mixes with the S1 phase. The S2 phase with long period signals appears significantly, but it cannot be identified on the waveform of the small earthquake. This signal appears in velocity records recorded from both the accelerometer and broadband instrument, indicating that it was not due to an instrument problem (drifting), as shown in Fig. S3. Furthermore, the consistency between the arrival times of P1 and S1 phases of the Meinong earthquake and those of the P and S phases of the E2008 event (Fig. 5a) indicates the hypocenter reported by CWB was the foreshock's hypocenter.

Fig. 6(b) shows the waveforms after applying a 0.33 Hz low-pass filter, a common filter typically used in finite-fault inversion. The P1 and S1 phases become rather small, and the largest phase (S2) of the Meinong earthquake is ~7 s later than the S phase of the E2008 earthquake. Therefore, in the case where the filter is applied, the Meinong earthquake seemingly appears to be a single event (the second event, mainshock) in the low-frequency band because the foreshock was buried due to the filtering. Several stations near the epicenter reported by CWB have the same characteristics as shown in Fig. S4. This again suggests the benefit from the dense seismic network from unfiltered data to discover earthquake source complexity.

For determining the focal mechanism of the foreshock, we apply a grid-search technique to determine what focal solution can make S-wave amplitude ratios in three components pairs (N/Z, N/E, and E/Z) of the synthetic waveforms explain the observed ones. We only analyze the unfiltered, clearly recorded S1 phases from 11 stations to the south. The synthetics are calculated by F-K modeling (Zhu and Rivera, 2002) with an average 1D velocity model beneath these southern stations (H14-1D-S) calculated from the H14-3D model (Table 1). The searching ranges of strike, dip, and rake are 250°–300°, 0°–90°, and -90°–90°, respectively. The best solution is given by strike/dip/rake = 275/20/15, which is close to the focal mechanism obtained by the RMT solution (276/22/20) (Lee et al., 2016) rather than the first motion solution (263/15/-18) by the CWB (Fig. S5).

Since the focal mechanism and hypocenter of the foreshock were determined, we simply compare the S1 phase amplitudes of observation and synthetic in a low-frequency, less than 0.33 Hz, in the MASB E-component to estimate the moment magnitude for the foreshock. The synthetic of the S1 phase is calculated by the F-K technique and the H14-1D-S velocity model with a triangular source time function for 1-second duration. We assume the contamination from the P2 phase was not significant. The reasonable moment magnitude of the foreshock is M_W 5.5 (Fig. S6). Compared to the total moment of the M_W 6.2 Meinong earthquake ($M_0 = 2.5\times10^{18}$ Nm) determined by the RMT solution, the moment of the foreshock ($M_0 = 2.2\times10^{17}$ Nm) was only ~10% of the total moment. It suggests that the waveforms in a low-frequency band might be dominated by the mainshock.

For the mainshock, we simply follow the solutions of the RMT solution since the waveforms in a low-frequency band should be dominated by the mainshock due to the large difference in size of both events. The moment of the mainshock (2.3×10^{18} Nm), which is calculated from the ratio of seismic moment against the foreshock, represents an M_W 6.18 event. The best double-couple solution was 276/22/20 and 167/83/111, shown in Figs. 1 and 5(a).

Discussion

Two independent events or two asperities?

A common question raised for a complex source such as the Meinong earthquake is: Are these two events two asperities on the same fault or two independent events? To answer the question, we discuss the results from three different viewpoints. 1) The similarity of the focal mechanisms: Two significantly different focal mechanisms may imply that two events have not occurred on the same fault plane. The result shown in the previous sections, however, indicates that the focal solutions for both events have little difference. Hence, we are not able to make a conclusion from the focal mechanisms alone. 2) Spatial and temporal separations: Considerable temporal or spatial separations between the two events may suggest the ruptures of these two events are disconnected. Our result shows that the centroids of the two events are ~12 km apart based on the location solutions from the SSA method and the epicenter location proposed by the CWB. Temporally, the delay time between the foreshock origin and the mainshock centroid is 5.3 s. Combining the spatial and temporal relationships between the two events and assuming the ruptures of the events are connected, the rupture velocity is approximately 2.31 km/s, which is slightly smaller than 0.8 times the S-wave velocity in the source region (Vs = 3.23 km/s, H14-3D model), 2.58 km/s, and is consistent with the rupture speed determined by the back projection technique (Jian et al., 2017). Therefore, from the second viewpoint, this event could be considered as two independent sources or two asperities on the fault, while the evidence is not strong enough to draw a conclusion. 3) The characteristics of the local seismic waveforms: Due to the fact that two clear P- and S-wave phase pairs are identified in the records from the southern stations (Figs. 3, 4, and 6), it might indicate the two ruptures were interrupted (the foreshock and the mainshock discussed in section "Location of the mainshock"), or, at least, slips between both the rupture areas were tiny. In other words, the Meinong earthquake is more likely composed of two independent events from this point of view. Another evidence to support the two independent events hypothesis is that both events occurred in the same depth of 15 km but had a large interval of 12 km horizontally. To combine both events on a fault, we might need a nearly horizontal fault plane, which might not be consistent with the focal mechanism solutions.

It is intriguing to discuss how these two events were triggered at once. Further studies on earthquake dynamic triggering might help address this question. In addition, the interrupted rupture behavior between both events indicates that the strong directivity effect might be related to the mainshock only. In the next section, we will focus on the mainshock and simulate the waveform of the velocity pulse-like ground motions, which produced serious damage in Tainan City.

Observations and modeling of the velocity pulse-like ground motions

Large velocity pulses were observed in the Meinong earthquake and were responsible for damaging buildings and for the fatalities, which are related to the mainshock, as identified at most stations near Tainan City in Fig. S7. The velocity pulses recorded from those stations indicate very large amplitude and narrow pulse widths in Fig. 7. The largest peak velocity was 101.2 cm/s with a period of 2 s, which appeared in the E-component in the station W21B. This large velocity pulse with the short duration is similar to other velocity pulses recorded by Mw 6.7 Northridge earthquake and Mw 6.6 San Fernando earthquake (Cox and Ashord 2002; Baker, 2007). We would like to directly simulate these large short-period velocity pulses without any filtering by considering the mainshock centroid information.

To model the velocity pulses shown in these stations, we consider an F-K modeling (Zhu and Rivera, 2002) for an average 1D structure (H14-1D-W) around Tainan City from the H14-3D model (Table 2), which includes a low S-wave velocity structure in the top 1000 m. The shallow structure was determined by microtremor analyses in the Western Plain of Taiwan described in Kuo et al. (2016). We consider the structure beneath the station CHY091, which is the nearest station of Tainan City as the shallow structure used in this study.

We consider variable durations of triangular source-time functions from 1.2 to 5.0 s and calculate the synthetic velocity waveforms for these stations by using the seismic moment of $M_0 = 2.3\times10^{18}$ Nm, or equivalent moment magnitude M_W 6.18, as well as the focal mechanism of the RMT solution for the mainshock. We then compare the width of the velocity pulses between the synthetics and observations in E-W component and obtain the best source duration for each station. The velocity pulse widths used for the comparisons are shown in T1 and T2 markers in Fig. 7(a). The results indicate that we can explain most of the velocity pulses well in both horizontal components in the stations near Tainan City (AZ=229°~279°) by a point source with a source-time function of 1.4-2.2 s (Figs. 8a and 8b). The average source duration of these stations is 1.7 s. Furthermore, synthetics from the source parameters also explain the observations in southern station MASB (AZ=163°) by using a wider source time duration of 4.5 s (Fig. 8). It suggests a strong directivity effect toward Tainan City produced heavy damages was due to the mainshock only. The results also indicate that the location, magnitude, and focal mechanism of the mainshock we estimated are reasonable.

Comparison of two-event sources and the finite-fault slip model

The finite-fault slip distribution model from waveform inversion has become a useful tool to quickly reveal the slip distribution on the fault after an earthquake. Compared to the results from our two-event sources model which analyzed unfiltered records and the finite-fault slip model which considered low-frequency geophysical records (Lee et al., 2016), the largest source slip patterns and their strong directivity effect toward west of the Meinong earthquake are quite similar. The results from Lee et al. (2016) indeed revealed a large asperity to the north

north-west similar to the location of the mainshock (Fig. 9a). Both independent analyses of the present study and the finite-fault inversion by using different data verified this source characteristic. However, the finite-fault centroid is 5 km deeper than the mainshock as shown in Fig. 9(b). It may be related to an assumption of a dipping fault plane toward north for the finite-fault inversion technique. The asperities have to be located on the fault plane by priori assumption. Since the centroid location is in the north compared to the hypocenter at a depth of 14.6 km, it became to be located at a depth of ~20 km consequentially.

As a finite-fault waveform inversion is often applied to filtered data, the waveforms emitted by independent sources overlapped after filtering and, thus, yield a continuous distribution in slips, therefore, the foreshock would be buried. The dense high-performance seismic array allows us to examine the earthquake sources through close observation. The result revealed in this study benefits from the dense high-quality strong motion array. This low-cost seismometer for the purpose of EEW is surprisingly well behaved to be able to give close observations to earthquake sources with less distortion of waveforms from filtering. It is indeed a worthy note on the future understanding of earthquake sources, especially linked to earthquake engineering, using the low-cost strong motion array.

Conclusions

Using the seismic records from the local density networks without any filter, we recognize that the Meinong earthquake can be separated into an M_W 5.5 foreshock and an M_W 6.18 mainshock. The P- and S-wave phases of the foreshock (P1 and S1) and mainshock (P2 and S2) were recognized clearly in the travel-time curves for the southern stations, which is backward from the rupture direction. The time delay of the mainshock centroid is approximately 5.3 s. The location of the foreshock is at the hypocenter estimated by the CWB. We located the mainshock centroid by applying the modified SSA technique. The result indicates that the mainshock centroid occurred 12.3 km north north-west of the foreshock where there is a blank zone of the aftershocks, which is consistent with the results from the finite-fault inversion. However, the depth of the mainshock was 15 km, which is shallower than the centroid location determined by finite-fault inversion. The focal mechanism of the foreshock is 276/22/20 in strike/dip/rake, which is similar to the mainshock. Due to the clear identification of the phases in dense strong motion stations, we believe that the foreshock and mainshock were individual earthquakes rather than two asperities on a fault plane. This non-negligible foreshock for the epicenter region would be buried once we apply a low-pass filter on data processing, commonly used in source properties studies. The velocity pulse-like ground motions, responsible for the extensive damage, could be explained solely from a single source in the mainshock, which were well modeled. The combination of the close-in distance, the strong directivity from the mainshock, and site effect resulted in large velocity pulses that struck Tainan City, causing the disastrous damage. Using a dense seismic network as a seismic array helps us delineate the earthquake sources directly and provides more delicate information for future understanding on earthquake dynamic triggering. With more advanced development on low-cost seismometers, in the future, the seismic array method could become an important tool in deciphering earthquake source complexity. And, the experience from this Meinong earthquake could be a classic.

Data and Resources

The strong-motion waveform records used in this study were obtained from the National Taiwan University (NTU), the Institute of Earth Sciences (IES) of Academia Sinica, and the Central Weather Bureau (CWB). The P-alert records used in this study are available to the public and can be downloaded from the NTU cloud disk (https://www.space.ntu.edu.tw/navigate/s/5CDFA7C2CFD7487FB84E2CE3F7376C33QQY, last accessed March 2016). The strong-motion records from IES and CWB used in this study can be obtained upon request from IES and CWB. The damage records used in this study is at http://data.tainan.gov.tw/dataset/0206-earthquake/resource/476c935a-1611-40f0-ae46-0b53fd588c1f (last accessed June 1 2017). Broadband Array in Taiwan for Seismology (BATS) solution is available at http://bats.earth.sinica.edu.tw, and Global Centroid Moment Tensor (GCMT) solution is maintained at http://www.globalcmt.org/CMTsearch.html. Central Weather Bureau (CWB) website can be accessed at http://www.cwb.gov.tw/eng/index.htm (last accessed March 2016). Seismic Analysis Code (SAC) is available at http://ds.iris.edu/files/sac-manual/ (last accessed July 2016). Frequency-Wavenumber (FK) synthetic seismogram package is available at http://www.eas.slu.edu/People/LZhu/home.html (last accessed June 1 2017).

Acknowledgments

We appreciate the helpful comments from Profs. Hiroo Kanamori, Victor C. Tsai, and Dr. Zachary E. Ross who helped us to improve this manuscript. We thank Dr. Hsin-Hua Huang at Institute of Earth Sciences (IES), Academia Sinica, Taiwan providing Taiwan 3D velocity structure. Thanks to Central Weather Bureau providing the RTD records and source parameters, including earthquake location and focal mechanism, of the Meinong earthquake. This research was supported by the Taiwan Earthquake Research Center (TEC), funded through the Ministry of Science and Technology (MoST) with grant number MOST 103-2628-M-001-004-MY3. The TEC contribution number for this article is xxxxx.

References

Baker, J. W. (2007). Quantitative classification of near-fault ground motions using wavelet analysis, *Bull. seism. Soc. Am.* **97**(5) 1486-1501 doi:10.1785/0120060255.

Cox, K. E., and S. A. Ashford (2002). Characterization of Large Velocity Pulses for Laboratory Testing. Report 2002/22, *Pacific Earthquake Engineering Research Center*. University of California, Berkeley, California, USA.

Duputel, Z., V. C. Tsai, L. Rivera, and H. Kanamori (2013). Using centroid time-delays to characterize source durations and identify earthquakes with unique characteristics, *Earth Planet. Sci. Lett.* **374** 92-100 doi:10.1016/j.epsl.2013.05.024.

Jian, P.-R, S.-H. Hung, L. Meng, and D. Sun (2017). Rupture characteristics of the 2016 Meinong earthquake revealed by the back-projection and directivity analysis of teleseismic broadband waveforms, *Geophys. Res. Lett.* **44** 3545-3553 doi: 10.1002/2017GL072552.

Kan, C.-W., H. Kao, G.-B. Ou, R.-Y. Chen, and C.-H. Chang (2010). Delineating the rupture planes of an earthquake doublet using Source-Scanning Algorithm: application to the 3 March 2005 Ilan doublet, northeast Taiwan, *Geophys. J. Int.* **182** 956–966.

Kanamori, H., L. Ye, B.-S. Huang, H.-H. Huang, S.-J. Lee, W.-T. Liang, Y.-Y. Lin, K.-F. Ma, Y.-M. Wu, and T.-Y. Yeh (2016). A strong-motion hot spot of the 2016 Meinong, Taiwan, earthquake (Mw=6.4), *Terr. Atmos. Oceanic Sci.* Accepted doi: 10.3319/TAO.2016.10.07.01.

Kao, H., and S.-J. Shan (2004). The Source-Scanning Algorithm: mapping the distribution of seismic sources in time and space, *Geophys. J. Int*. **157** 589–594.

Kao, H. and S.-J. Shan (2007). Rapid identification of earthquake rupture plane using Source-Scanning Algorithm, *Geophys. J. Int*. **168** 1011–1020.

Kao, H., K. Wang, R.-Y. Chen, I. Wada, J. He, and S. D. Malone (2008). Identifying the rupture plane of the 2001 Nisqually, Washington, earthquake, *Bull. seism. Soc. Am*. **98** 1546–1558.

Kao, H., C.-W. Kan, R.-Y. Chen, C.-H. Chang, A. Rosenberger, T.-C. Shin, P.-L. Leu, K.-W. Kuo, and W.-T. Liang (2012). Locating, monitoring, and characterizing typhoon-induced landslides with real-time seismic signals, *Landslides* **9** 557-563 doi:10.1007/s10346-012-0322-z.

Kuo, C.-H., C.-T. Chen, C.-M. Lin, K.-L. Wen, J.-Y. Huang, and S.-C. Chang (2016). S-wave velocity structure and site effect parameters derived from microtremor arrays in the Western Plain of Taiwan, *J. Asian Earth Sci.* 128 27-41 doi:10.1016/j.jseaes.2016.07.012.

Lee, S.-J., T-Y. Yeh, and Y.-Y. Lin (2016). Anomaly large ground shaking caused by constructive source rupture and wave propagation effects during the 6 February 2016 Meinong, Taiwan, M6.6 earthquake, *Seismol. Res. Lett.* **87**(6) 1319-1326 doi: 10.1785/0220160082

Liao, Y-C., H. Kao, A. Rosenberger, S.-K. Hsu, and B.-S. Huang (2012). Delineating complex spatiotemporal distribution of earthquake aftershocks: an improved Source-Scanning

Algorithm, *Geophys. J. Int.* **189** 1753–1770 doi: 10.1111/j.1365-246X.2012.05457.x

Hall, J. F., T. H. Heaton, M. W. Halling, and D. J. Wald (1995). Near-Source Ground Motion and its Effects on Flexible Buildings, *Earthquake Spectra.***11**(4) 569-605.

Heaton, T. H., J. F. Hall, D. J. Wald, and M. W. Halling (1995). Response of high-rise and base-isolated buildings to hypothetical Mw 7.0 blind thrust earthquake, *Science* **267** 206–211.

Huang, H.-H., Y.-M. Wu, C.-H. Chang, S.-J. Lee, T.-M. Chang, and H.-H. Hsieh (2014). Joint Vp and Vs tomography of Taiwan: Implications for subduction-collision orogeny, *Earth Planet. Sci. Lett.* **392** 177-191.

Shahi, S. K., and J. W. Baker (2011), An empirically calibrated framework for including the effects of near-fault directivity in probabilistic seismic hazard analysis, *Bull. seism. Soc. Am.* **101**(2) 742-755 doi: 10.1785/0120100090.

Somerville, P. G., N. F. Smith, R. W. Graves, and N. A. Abrahamson (1997). Modification of empirical strong ground motion attenuation relations to include the amplitude and duration effects of rupture directivity, *Seismol. Res. Lett.* **68**(1) 199-222.

Somerville, P. G. (2003). Magnitude scaling of the near fault rupture directivity pulse, *Phys, Earth Planet In*. **137** 201-212.

Wu, Y.-M., D.-Y. Chen, T.-L. Lin, C.-Y. Hsieh, T.-L. Chin, W.-Y. Chang, W.-S. Li, and S. H.

Ker (2013). A high density seismic network for earthquake early warning in Taiwan based on low cost sensors, *Seismo. Res. Let.* **84** 1048-1054, doi: 10.1785/0220130085.

Wu, Y.-M., W.-T. Liang, H. Mittal, W.-A. Chao, C.-H. Lin., B.-S. Huang, and C.-M. Lin (2016). Performance of a low-cost earthquake early warning system (P-alert) 1 during 2016 ML6.4 Meinong (Taiwan) earthquake, *Seismol. Res. Lett.* **87**(5) doi: 10.1785/0220160058.

Zhu, L., and L. A. Rivera (2002). A note on the dynamic and static displacements from a point source in multi-layered media, *Geophys. J. Int.* **148** 619-627 doi:10.1046/j.1365-246X.2002.01610.x.

Full mailing address for each author

Dr. Yen-Yu Lin

1200 E California Blvd., MS 252-21, Pasadena, CA 91125, USA

Mr. Te-Yang Yeh

5500 Campanile Drive, San Diego, CA 92182, USA

Dr. Kuo-Fong Ma

No.300, Jhongda Rd., Jhongli District, Taoyuan City, 32001 Taiwan (R.O.C.)

Dr. Teh-Ru Alex Song

Gower Street, London, WC1E 6BT, UK

Dr. Shiann-Jong Lee

128, Sec. 2, Academia Road, Nangang, Taipei, 11529 Taiwan (R.O.C.)

Dr. Bor-Shouh Huang

128, Sec. 2, Academia Road, Nangang, Taipei, 11529 Taiwan (R.O.C.)

Dr. Yih-Min Wu

No. 1, Sec. 4, Roosevelt Road, Taipei, 106 Taiwan (R.O.C.)

“Now at” affiliation

Yen-Yu Lin

Seismological Laboratory, California Institute of Technology, Pasadena, USA

Te-Yang Yeh

Department of Geological Sciences, San Diego State University, San Diego, USA, and

Scripps Institution of Oceanography, University of California, San Diego, USA

Table 1. The layer crustal structure, H14-1D-S, for the stations in the south

Layer	*H*(km)	*V*p(km/s)	*V*s(km/s)	ρ(g/cm3)	*Q*p	*Q*s
1	0.5	3.50	1.99	2.4	600	300
2	2.5	4.41	2.65	2.4	600	300
3	3.0	5.01	3.03	2.5	600	300
4	4.0	5.43	3.22	2.6	600	300
5	5.0	5.77	3.29	2.6	600	300
6	5.0	5.82	3.30	2.6	600	300
7	5.0	5.99	3.41	2.6	600	300
8	5.0	6.44	3.63	2.6	600	300
9	5.0	6.96	3.94	2.6	600	300
10	5.0	7.54	4.25	2.7	600	300
11	5.0	7.74	4.50	2.7	600	300
12	5.0	7.97	4.53	2.7	600	300
13	5.0	8.24	4.54	2.7	600	300

The average 1D velocity structure was determined from the H14-3D model (Huang et al., 2014) in the area within longitude E120.60°–120.80° and latitude N22.50°–23.00° near the distribution of the stations in the south.

Table 2. The crustal structure, H14-1D-W, for the stations in Tainan City

Layer	*H*(km)	*V*p(km/s)	*V*s(km/s)	*ρ*(g/cm3)	*Q*p	*Q*s
1	0.3	1.50	0.40	2.2	40	20
2	0.3	1.70	0.60	2.2	80	40
3	0.15	2.70	1.00	2.3	200	100
4	0.25	3.00	1.40	2.3	200	100
5	2.0	3.92	2.21	2.4	600	300
6	3.0	4.30	2.35	2.4	600	300
7	4.0	4.70	2.52	2.5	600	300
8	5.0	5.26	2.82	2.5	600	300
9	5.0	5.81	3.28	2.6	600	300
10	5.0	6.16	3.58	2.6	600	300
11	5.0	6.54	3.77	2.6	600	300
12	5.0	6.98	4.05	2.7	600	300
13	5.0	7.56	4.37	2.7	600	300
14	5.0	7.89	4.57	2.7	600	300
15	5.0	7.91	4.60	2.7	600	300

16	5.0	7.99	4.62	2.7	600	300

The average 1D velocity structure was determined from the H14-3D model (Huang et al., 2014) in the area near Tainan City within longitude E120.10°–120.50° and latitude N22.75°–23.20°. The shallow structure was determined by microtremor analyses in the Western Plain of Taiwan described in Kuo et al. (2016). We consider the structure beneath the station CHY091 which is the nearest station of Tainan City as the shallow structure used in this study.

Figure Captions

Figure 1. Map view of the Meinong earthquake epicenter, nearby metropolitan cities, and seismic station distribution. The red star is the epicenter reported by the CWB. The solutions of focal mechanism from the first motion (CWB), real-time moment tensor inversion (RMT), and W-phase inversion (W-phase) are shown in the figure. The red circles represent three big cities in southern Taiwan. The triangles, diamonds, and squares indicate the stations of BATS, RTD, and P-alert, respectively. The stations with a red frame denote the travel-time curves plotting in Fig. 3. The station names in red, green, orange, and blue are for the layouts of the stations in the south, west, east, and north, respectively, in Fig. 4. The black square reveals the area in Fig. 5. The red circles demonstrate seriously damaged buildings due to the Meinong earthquake. The black lines reveal surface tracks for known faults in southern Taiwan.

Figure 2. The distribution of the peak-ground acceleration (PGA) and peak-ground velocity (PGV). The damaged buildings and the P-alert stations are shown in green squares and black dots, respectively. The white and blue stars are the locations of the mainshock centroid (SSA) and epicenter (CWB), respectively.

Figure 3. (a-c) The record sections of the vertical, and the two horizontal components from the southern stations with a red frame mentioned in Fig. 1. The amplitudes of each trace are

normalized by the maximum amplitude. The moveout of S2 is revealed by the gray dashed lines. (d-f) The same record sections while each trace only shows up to 20% of the maximum amplitude in order to demonstrate P-waves clearly. The P2 phases are marked by the solid gray lines. The T1 and T2 markers are the P- and S-wave arrival times calculated by the H14-3D model (P1 and S1 phases). (g) The picked travel-time curves of P- and S-wave pairs for the foreshock and the mainshock are shown in thin and thick dashed lines, respectively

Figure 4. Displacement waveforms of the E-component of the stations in the (a) south, (b) west, (c) east, and (d) north. The blue dots indicate the P1 and S1 phases for the foreshock. The yellow circles are P2 and S2 phases for the mainshock. The waveform in red is the contribution of the S2 phase in each trace. The station name, distance, and azimuth are indicated on the traces.

Figure 5. (a) Probabilities distribution of the mainshock centroid in the map view and (b) E-W-depth profile. The color scale indicates probability of the mainshock centroid in the location. The green star, diamond, triangle, inverse triangle, and pentagon reveal the solutions from the CWB, P-alert, RMT, GCMT, and W-phase, respectively. The purple circle is the location of the small earthquake (E2008). The focal mechanisms of W-phase and RMT for the Meinong earthquake and for the E2008 earthquake are

revealed in the figure. The comparison of the first motion and grid search solutions of the foreshock are shown on the figure. The station MASB and the fully collapsed building are marked in a purple square and black X, respectively. The black triangles are the strong motion stations used in the study. (c) Marginal probability with delay time. The maximum probability is marked with an open circle in 6.1 s.

Figure 6. (a) Comparison of the E-component waveforms for the Meinong earthquake and the E2008 event (M_W 5.05) from the MASB station. (b) The waveforms apply a low-pass filter of 0.33 Hz. The arrivals of the P1, S1, P2, and S2 phases are indicated on the traces of the 2016 Meinong earthquake. The E2008 event's P- and S-wave arrivals are demonstrated on its traces.

Figure 7. Observable (lines in black) and synthetic (lines in red) velocity waveforms in (a) E-component and (b) N-component for the stations in Tainan City. The durations of the velocity pulses for the comparisons are marked in T1 and T2 markers. The source duration used for each synthetic is shown on the trace.

Figure 8. Observed (lines in black) and synthetic (lines in red) velocity waveforms for three components of the MASB station. The source-time duration for the waveform simulations is 4.5 s. The synthetics were calculated by using the H14-1D-S model.

Figure 9. Comparison of the two-sources model described in the present study and the co-seismic slip distribution described in Lee et al.'s (2016) study (black counters). The black circles indicate the aftershocks of the 2016 Meinong earthquake. The green and red stars are the locations of the mainshock centroid (SSA) and epicenter (CWB), respectively. The green circle denotes the centroid from the finite-fault inversion. The color scale indicates the co-seismic slip determined by the finite-fault inversion. (b) Comparison of the mainshock centroid and the finite-fault centroid. The black line indicates the assumed fault plane used in the finite-fault inversion. The blue star, green circle, and open star demonstrate the hypocenter of the foreshock, the finite-fault centroid, and the mainshock centroid, respectively. The color scale indicates the probability of the mainshock centroid.

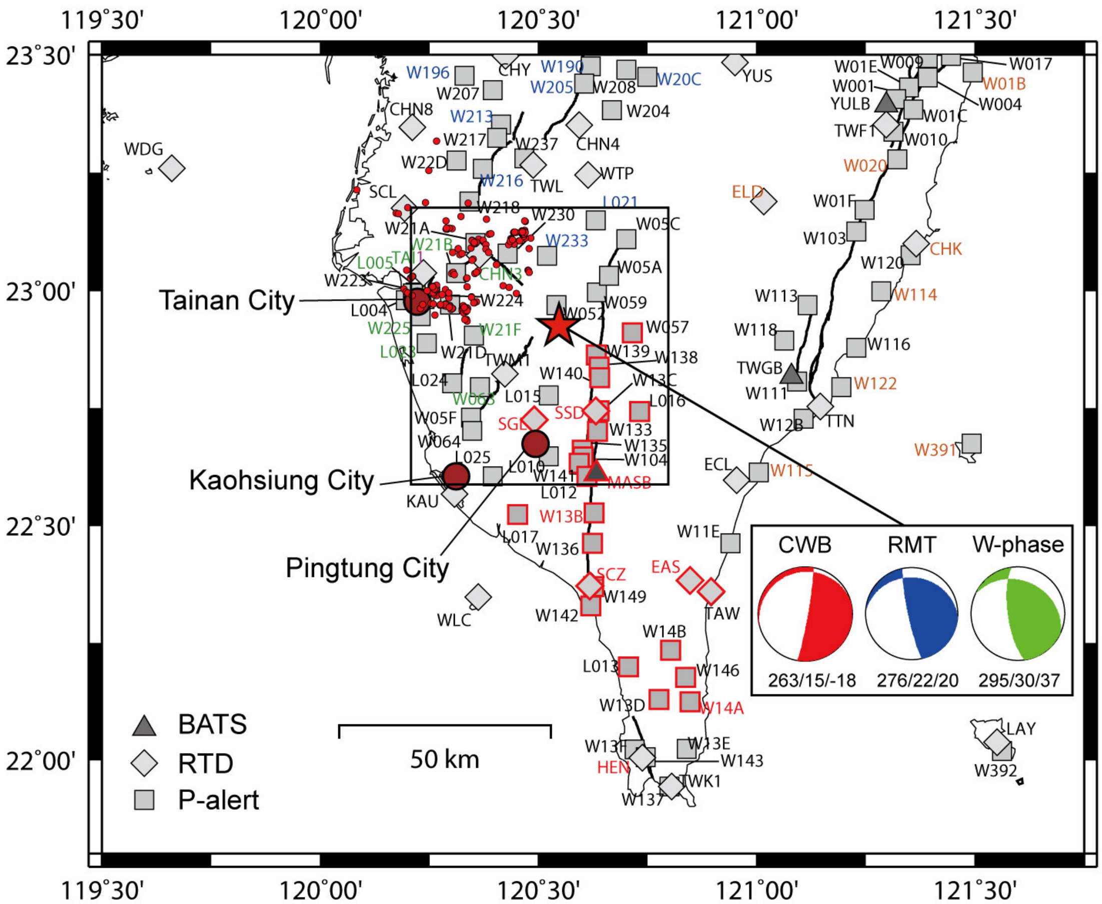

Figure 1. Map view of the Meinong earthquake epicenter, nearby metropolitan cities, and seismic station distribution. The red star is the epicenter reported by the CWB. The solutions of focal mechanism from the first motion (CWB), real-time moment tensor inversion (RMT), and W-phase inversion (W-phase) are shown in the figure. The red circles represent three big cities in southern Taiwan. The triangles, diamonds, and squares indicate the stations of BATS, RTD, and P-alert, respectively. The stations with a red frame denote the travel-time curves plotting in Fig. 3. The station names in red, green, orange, and blue are for the layouts of the stations in the south,

west, east, and north, respectively, in Fig. 4. The black square reveals the area in Fig. 5. The red circles demonstrate seriously damaged buildings due to the Meinong earthquake. The black lines reveal surface tracks for known faults in southern Taiwan.

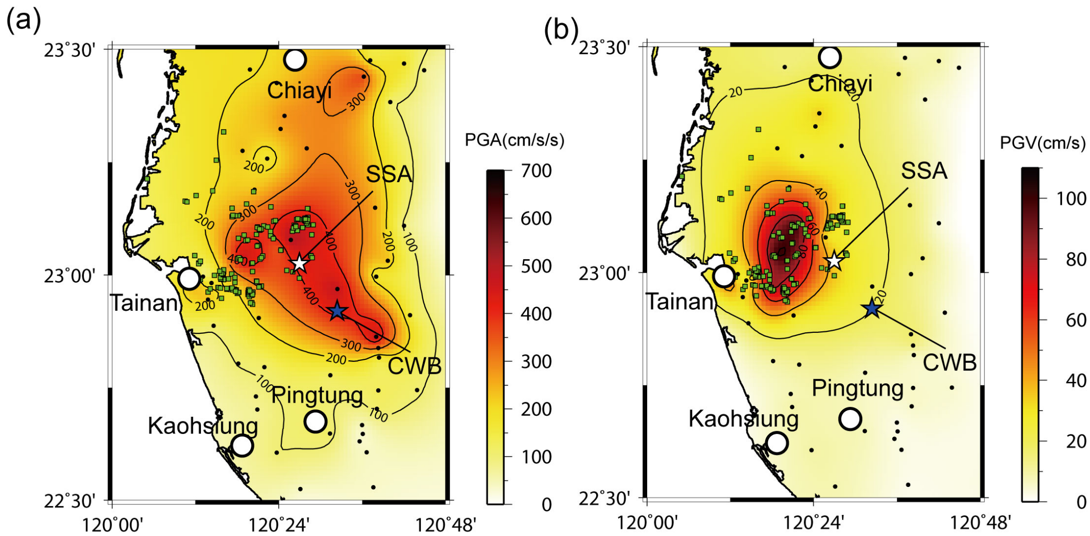

Figure 2. The distribution of the peak-ground acceleration (PGA) and peak-ground velocity (PGV). The damaged buildings and the P-alert stations are shown in green squares and black dots, respectively. The white and blue stars are the locations of the mainshock centroid (SSA) and epicenter (CWB), respectively.

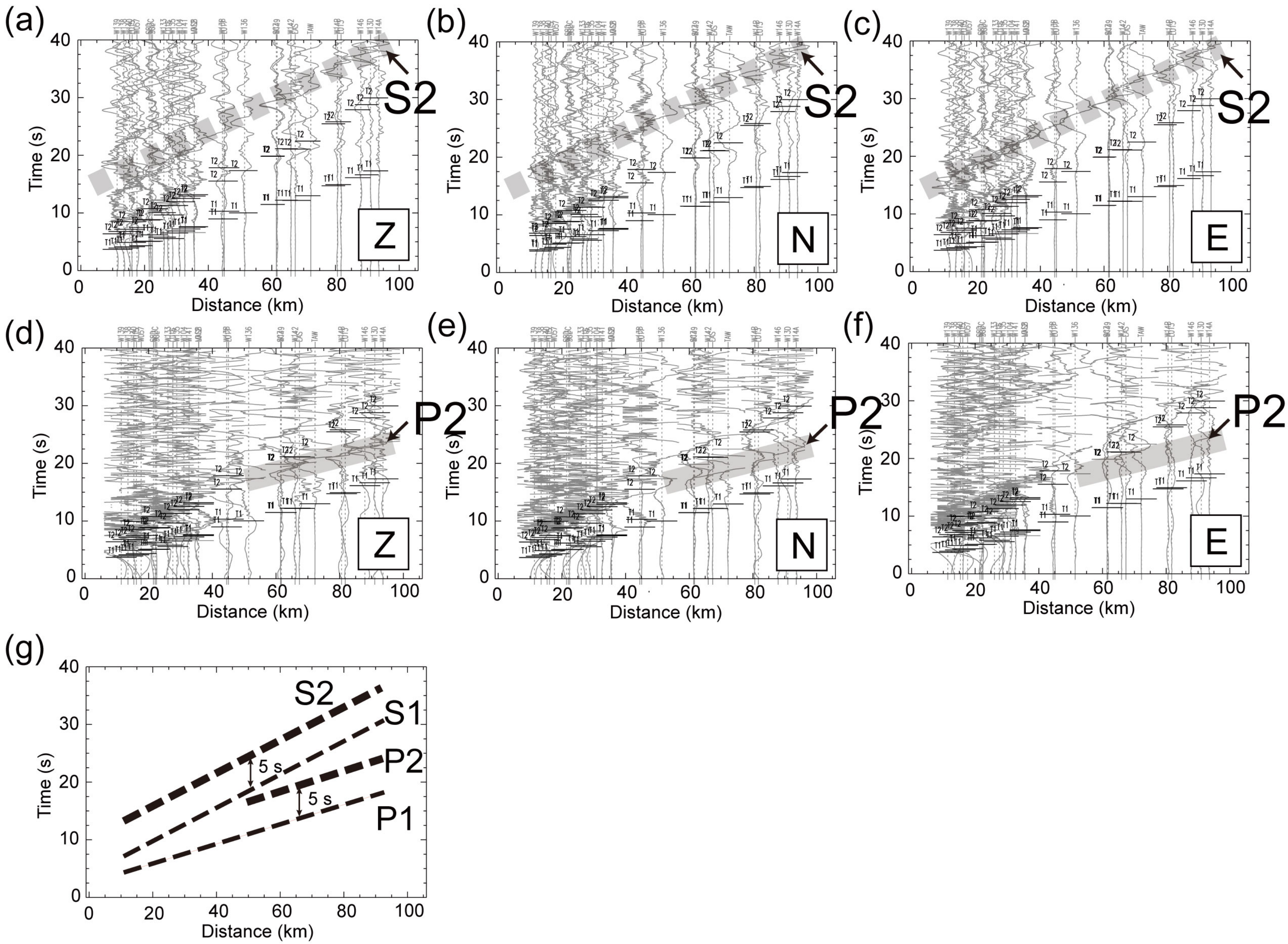
(a)
(b)
(c)
(d)
(e)
(f)
(g)
Time (s)
Distance (km)
S2
P2
Z
N
E
S1
P1
5 s

Figure 3. (a-c) The record sections of the vertical, and the two horizontal components from the southern stations with a red frame mentioned in Fig. 1. The amplitudes of each trace are normalized by the maximum amplitude. The moveout of S2 is revealed by the gray dashed lines. (d-f) The same record sections while each trace only shows up to 20% of the maximum amplitude in order to demonstrate P-waves clearly. The P2 phases are marked by the solid gray lines. The T1 and T2 markers are the P- and S-wave arrival times calculated by the H14-3D model (P1 and S1 phases). (g) The picked travel-time curves of P- and S-wave pairs for the foreshock and the mainshock are shown in thin and thick dashed lines, respectively

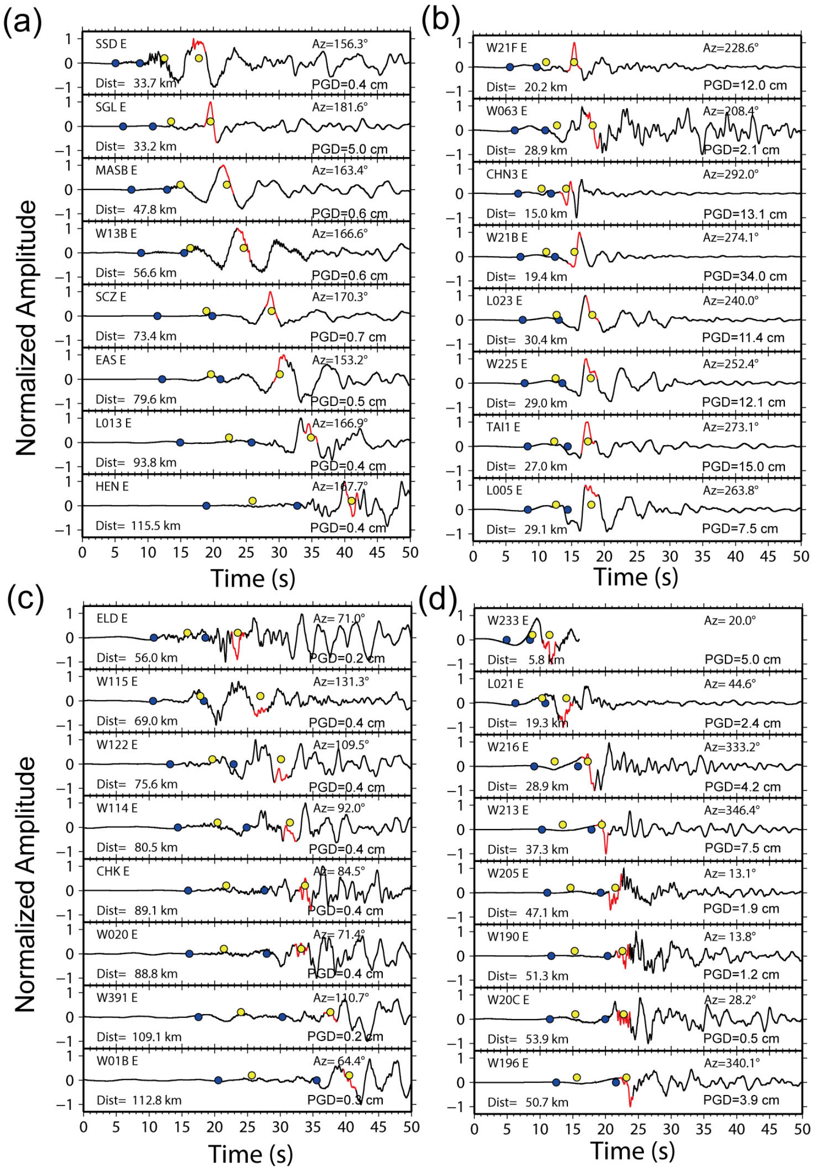

Figure 4. Displacement waveforms of the E-component of the stations in the (a) south, (b) w (c) east, and (d) north. The blue dots indicate the P1 and S1 phases for the foreshock. The y circles are P2 and S2 phases for the mainshock. The waveform in red is the contribution of S2 phase in each trace. The station name, distance, and azimuth are indicated on the traces.

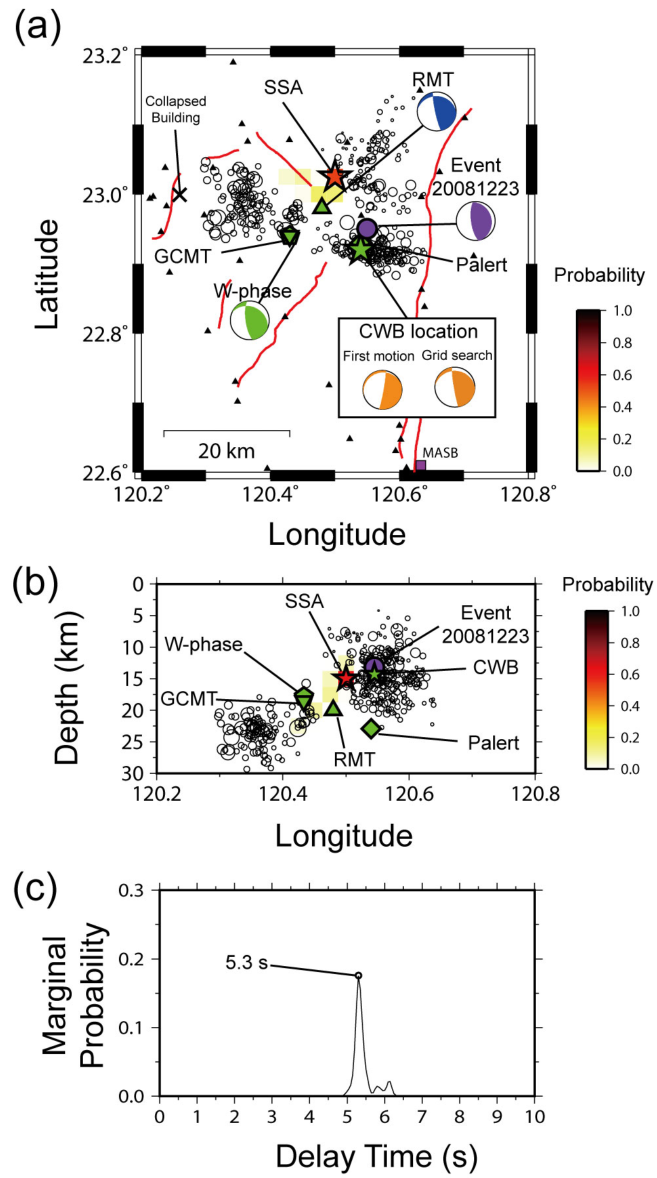

Figure 5. (a) Probabilities distribution of the mainshock centroid in the map view and (b) E-W-depth profile. The color scale indicates probability of the mainshock centroid in the location. The green star, diamond, triangle, inverse triangle, and pentagon reveal the solutions from the CWB, P-alert, RMT, GCMT, and W-phase, respectively. The purple circle is the location of the small earthquake (E2008). The focal mechanisms of W-phase and RMT for the

Meinong earthquake and for the E2008 earthquake are revealed in the figure. The comparison of the first motion and grid search solutions of the foreshock are shown on the figure. The station MASB and the fully collapsed building are marked in a purple square and black X, respectively. The black triangles are the strong motion stations used in the study. (c) Marginal probability with delay time. The maximum probability is marked with an open circle in 5.3 s.

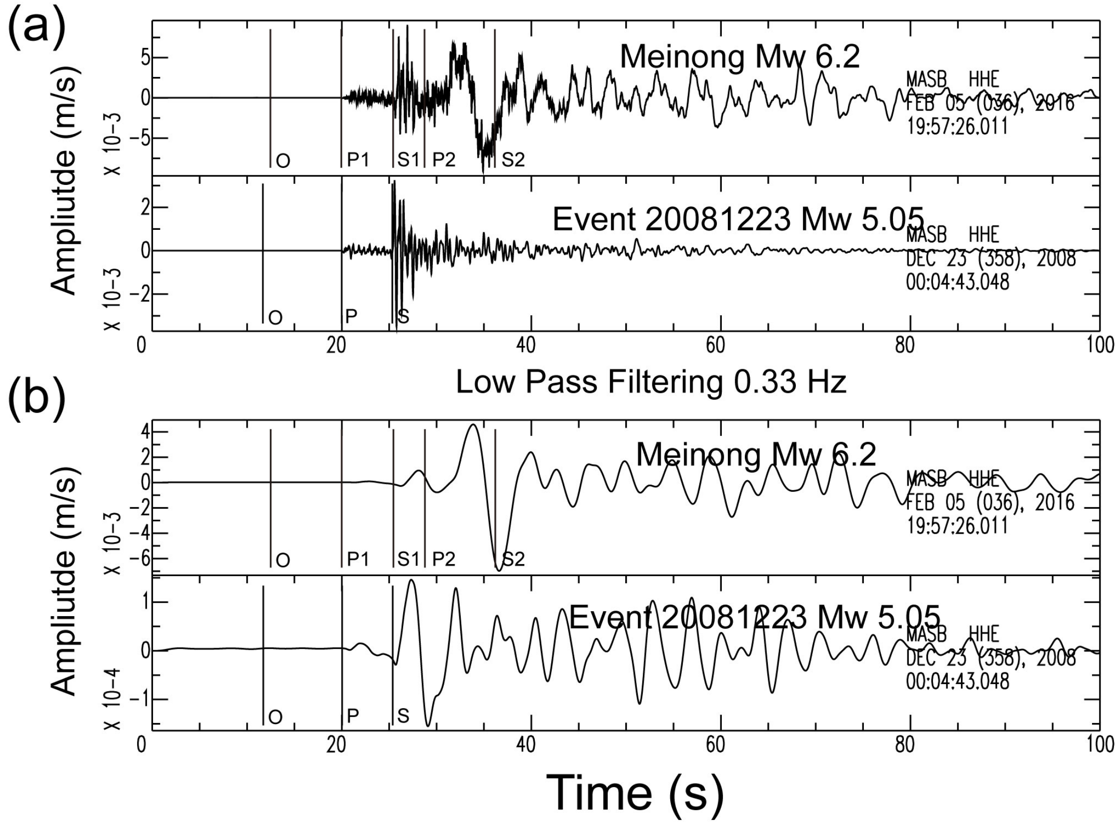

Figure 6. (a) Comparison of the E-component waveforms for the Meinong earthquake and the E2008 event (M_W 5.05) from the MASB station. (b) The waveforms apply a low-pass filter of 0.33 Hz. The arrivals of the P1, S1, P2, and S2 phases are indicated on the traces of the 2016 Meinong earthquake. The E2008 event's P- and S-wave arrivals are demonstrated on its traces.

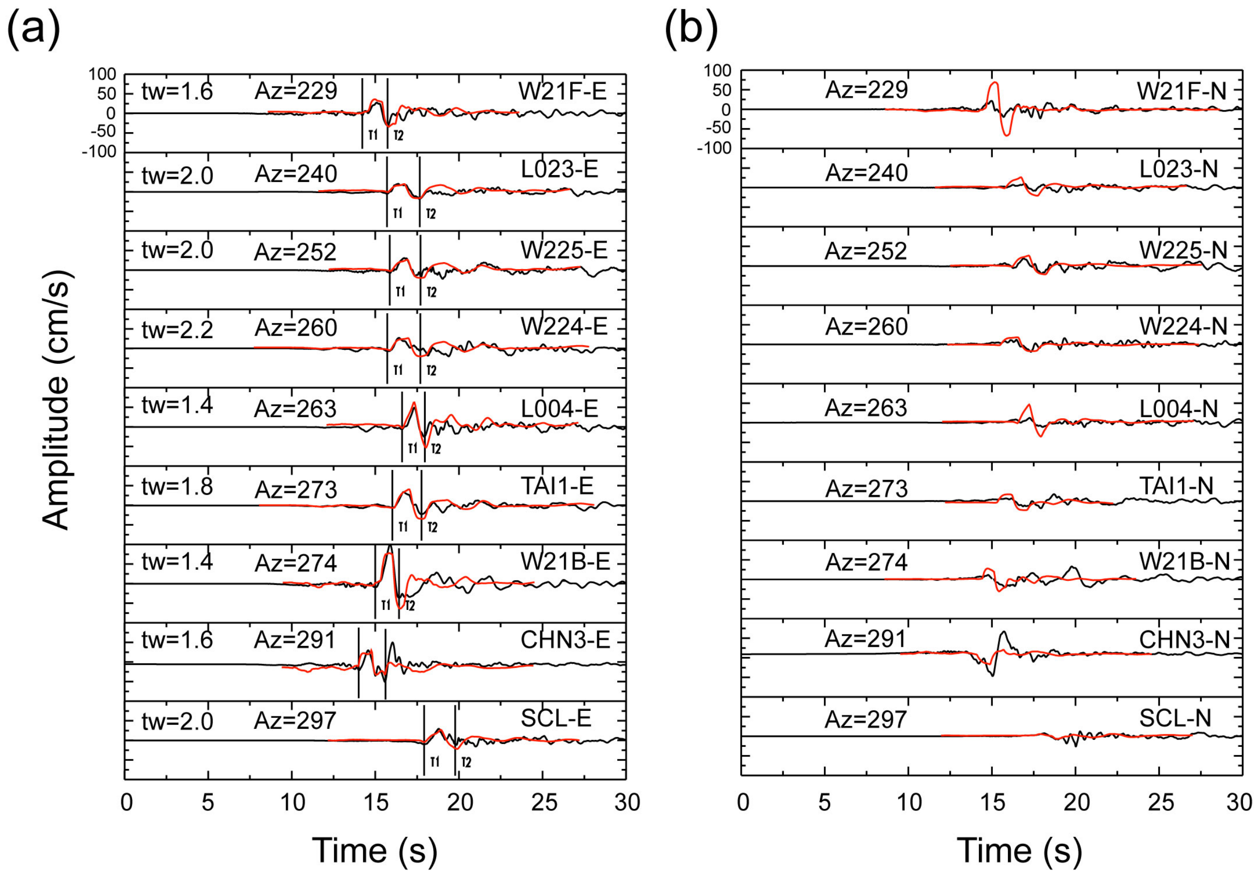

Figure 7. Observable (lines in black) and synthetic (lines in red) velocity waveforms in (a) E-component and (b) N-component for the stations in Tainan City. The durations of velocity pulses for the comparisons are marked in T1 and T2 markers. The best source duration used for each synthetic is shown on the trace.

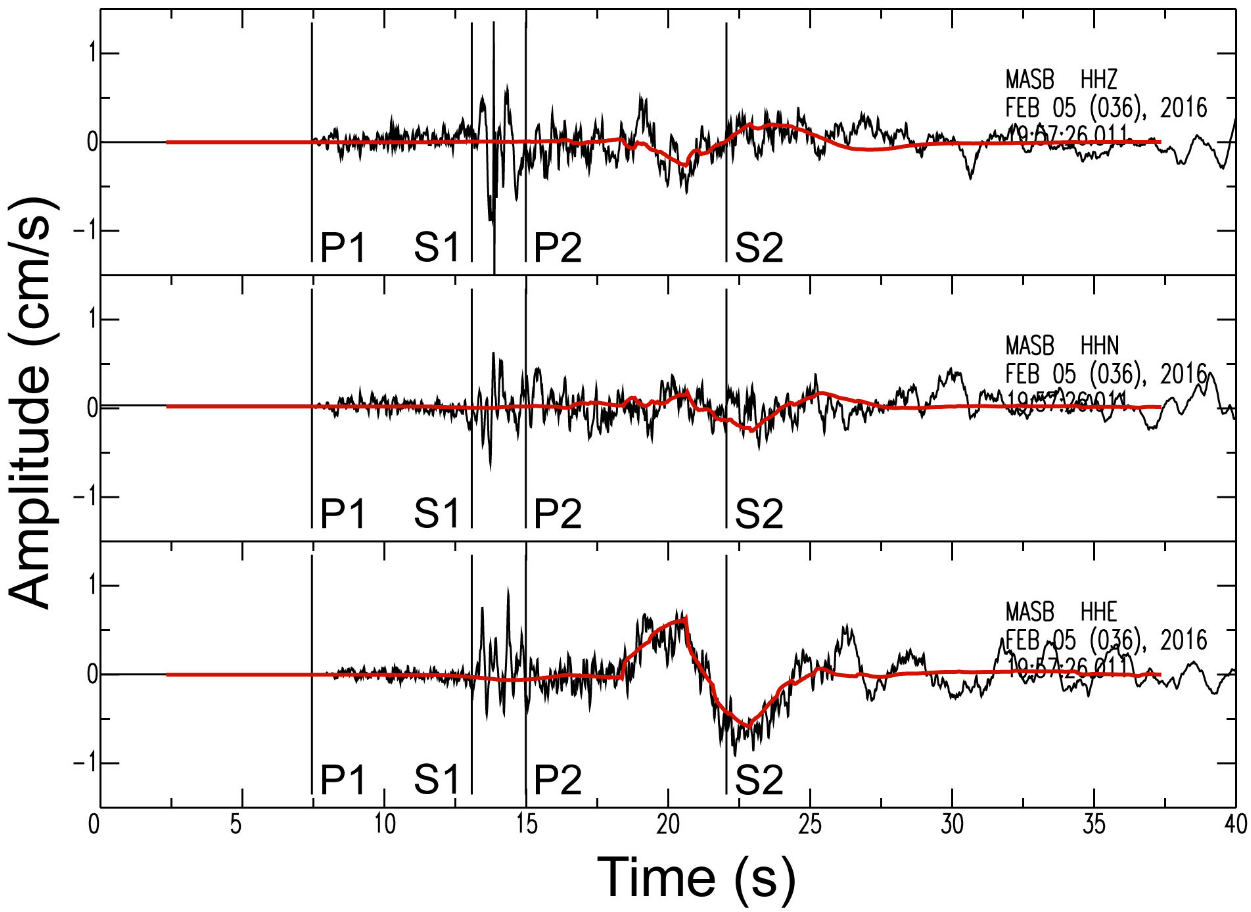

Figure 8. Observed (lines in black) and synthetic (lines in red) velocity waveforms for three components of the MASB station. The source-time duration for the waveform simulations is 4.5 s. The synthetics were calculated by using the H14-1D-S model.

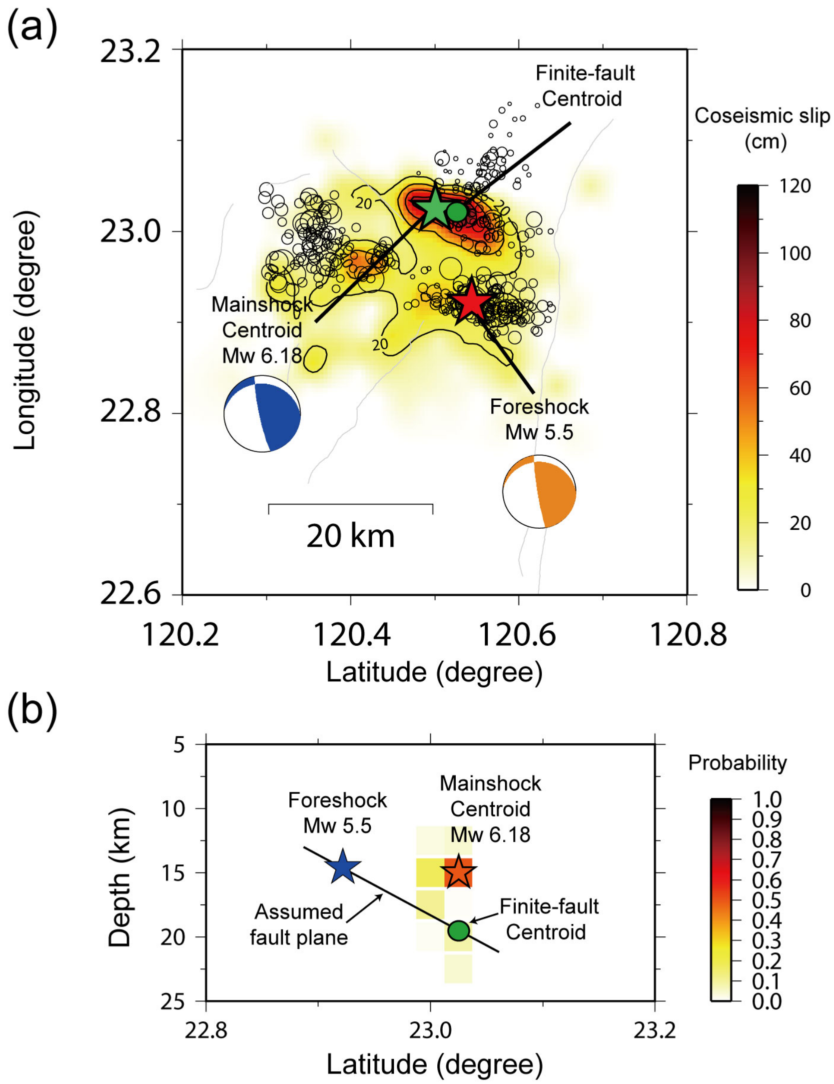

Figure 9. (a) Comparison of the two-sources model described in the present study and the co-seismic slip distribution described in Lee et al.'s (2016) study (black counters). The black circles indicate the aftershocks of the 2016 Meinong earthquake. The green and red stars are the locations of the mainshock centroid (SSA) and epicenter (CWB), respectively. The green circle denotes the centroid from the finite-fault inversion. The color scale indicates the co-seismic slip determined by the finite-fault inversion. (b) Comparison of the mainshock centroid and the

finite-fault centroid. The black line indicates the assumed fault plane used in the finite-fault inversion. The blue star, green circle, and open star demonstrate the hypocenter of the foreshock, the finite-fault centroid, and the mainshock centroid, respectively. The color scale indicates the probability of the mainshock centroid.

Supplementary to

Source Characteristics of the 2016 Meinong (M_L 6.6), Taiwan, Earthquake, Revealed from Dense Seismic Arrays: Double Sources and Velocity Pulse-like Ground Motion

by Yen-Yu Lin, Te-Yang Yeh, Kuo-Fong Ma, Teh-Ru Alex Song, Shiann-Jong Lee, Bor-Shouh Huang, Yih-Min Wu

This electronic supplement contains seven figures. This electronic supplement contains seven figures, including the resolution test of the improved SSA method (Fig. S1); the comparison of the results between the improved and original SSA methods (Fig. S2); the comparison of waveforms recorded by an accelerometer and a broadband instrument at the MASB station (Fig. S3); the comparison of unfiltered and filtered waveforms of the stations in the south (Fig. S4); the observed waveforms and the predicted synthetic waveforms considering different focal mechanisms for the foreshock (Fig. S5); the comparison of the observations and synthetic waveforms considering M_W 5.5 for the foreshock (Fig. S6); distribution of the stations record the large velocity pulse-like ground motions (Fig. S7).

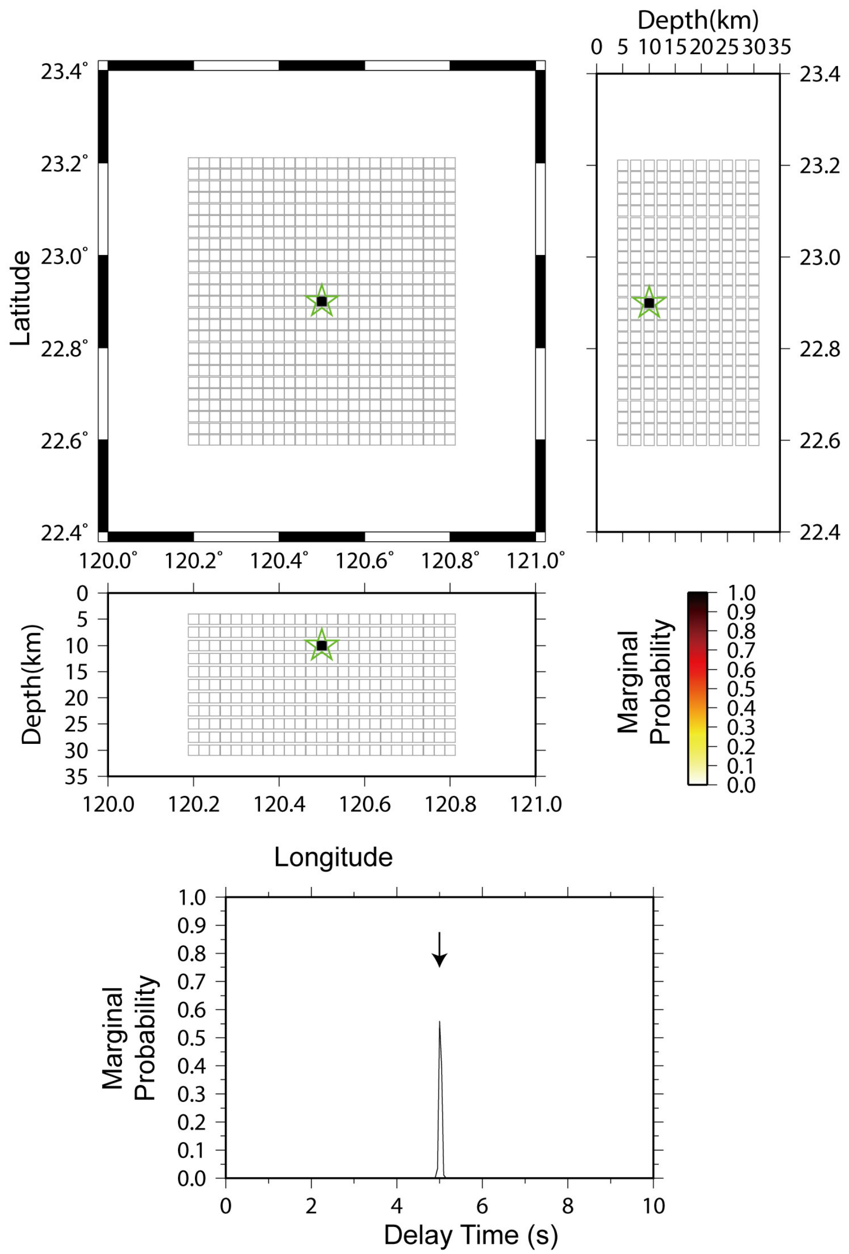

Figure S1. Synthetic test resolution for the improved SSA method. Upper and lower sections demonstrate the spatial and temporal resolution results, respectively. The green stars in the upper section are the input location and the arrow in the lower section is the input centroid delay time.

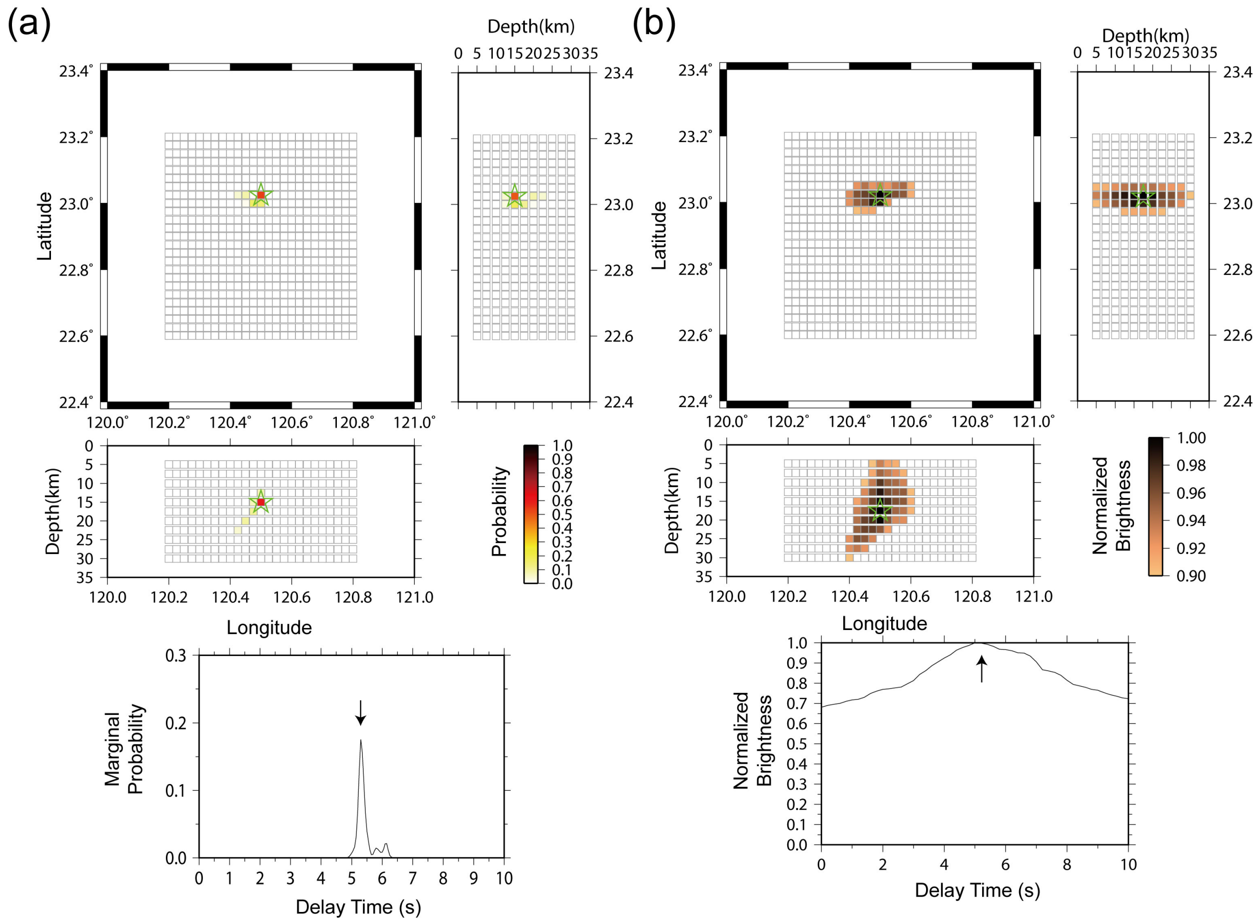

Figure S2. Comparison of the (a) improved and (b) original SSA methods. The upper section and lower sections demonstrate the spatial and temporal resolution results, respectively. The green stars in the upper section reveal the best solution of the mainshock. The arrows in the lower section are the best solution for the centroid delay. The color bar in (a) indicates marginal probability, and the color bar in (b) obtains normalized brightness.

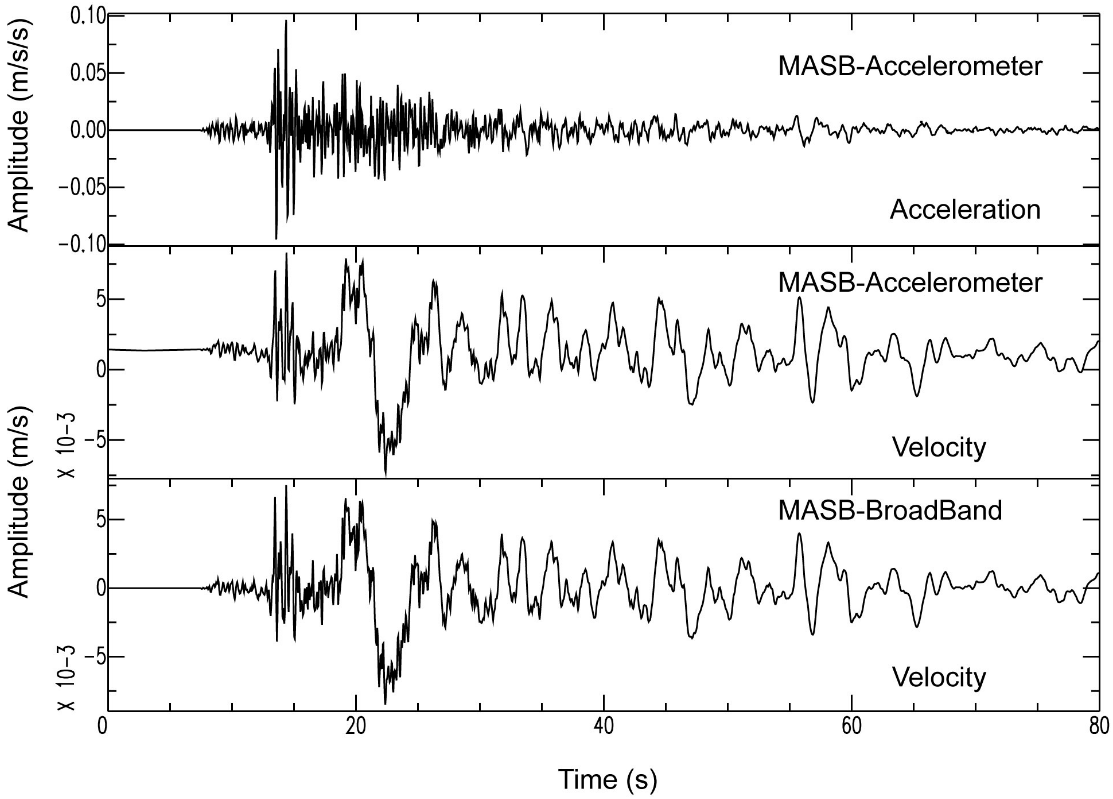

Figure S3. Comparison of the velocity waveforms from the accelerometer and broadband instrument in the MASB station. No filter was applied in the records.

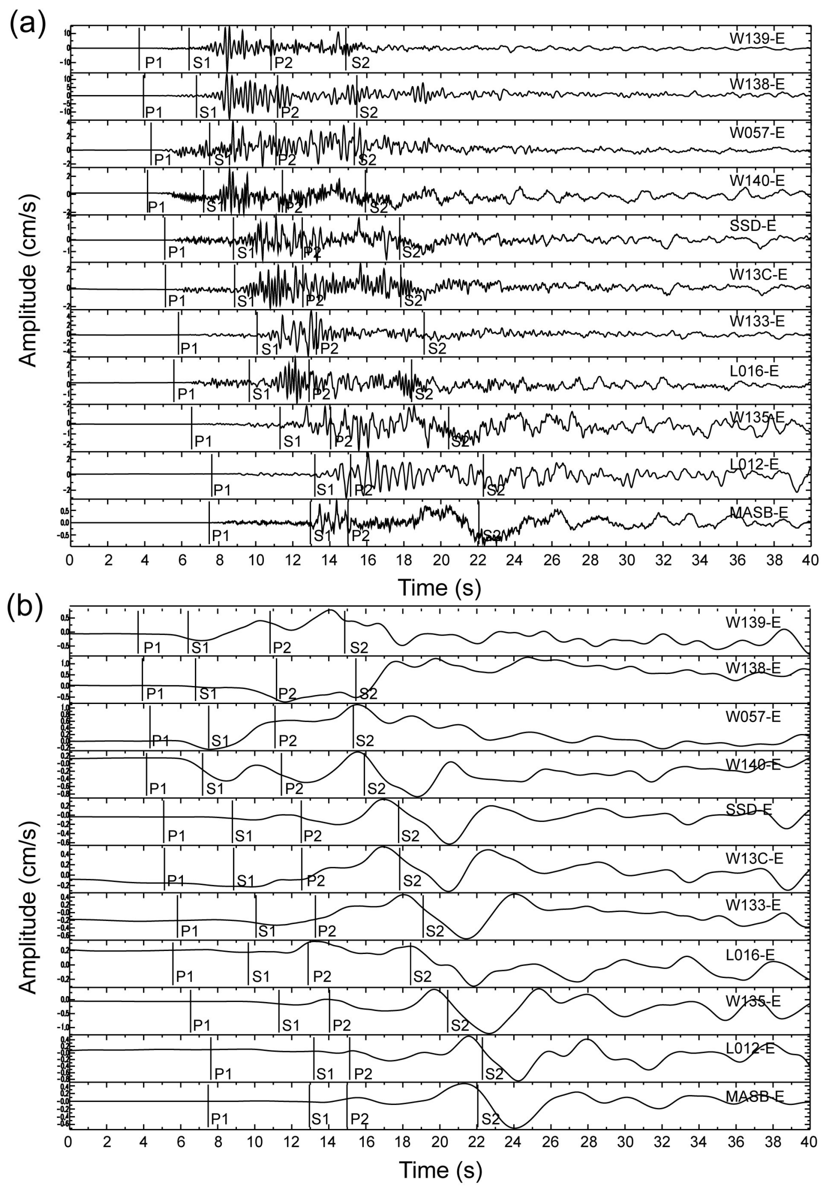

Figure S4. Comparison of (a) original velocity E-component waveforms and (b) the waveforms apply a low-pass filter of 0.33 Hz for the stations in the south of the hypocenter. The arrivals of the P1, S1, P2, and S2 phases are indicated on the traces.

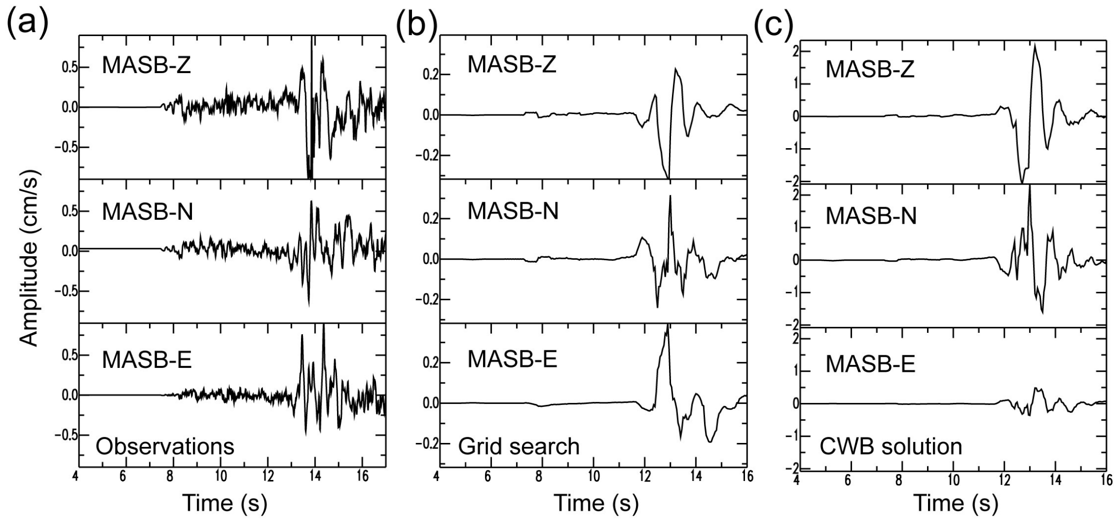

Figure S5. Comparison of (a) the velocity observations and (b-c) synthetics for the foreshock in the MASB station. The synthetics are considered the focal mechanism from (b) the grid search (275/20/15) and (c) the CWB focal solution (263/15/-18). No filter was applied in the records.

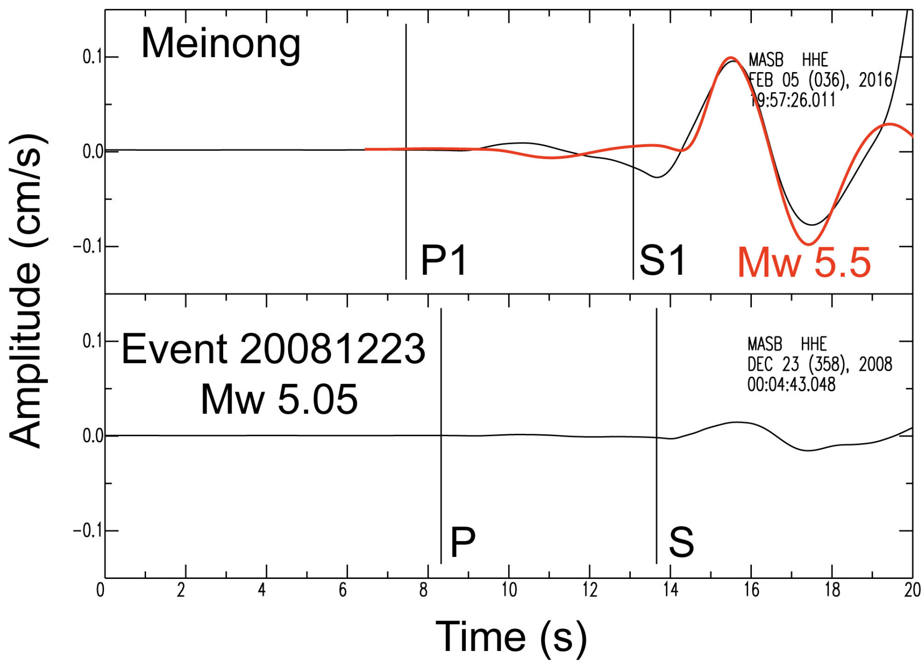

Figure S6. Comparison of the observation (black line in the upper section) and the S1-phase synthetic (red line) considering the foreshock's source parameters (the CWB hypocenter, M_W 5.5, and the focal mechanism 275/20/15) in the MASB records in the E-component. The lower section indicates the observation of the E2008 event M_W 5.05 as a reference. A low-pass filter of 0.33 Hz was applied in all records.

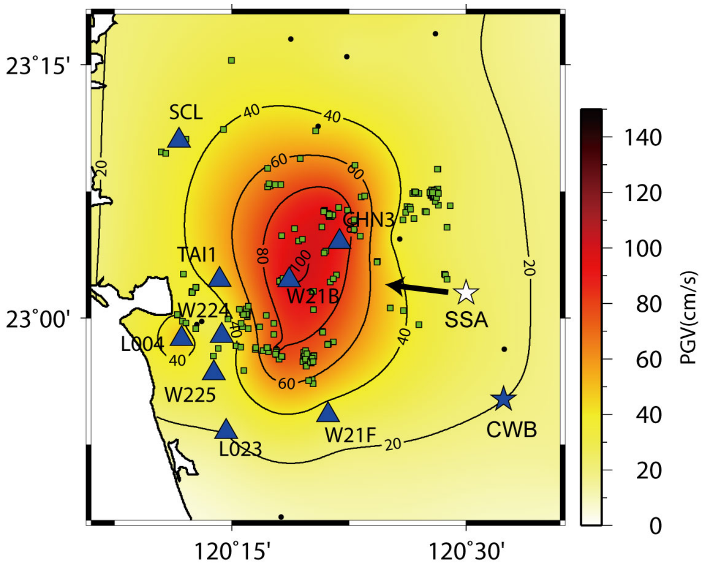

Figure S7. Distribution of the stations recorded the large velocity pulse-like ground motions near Tainan City.